Plastic deformation mechanisms in BCC single crystals and equiatomic alloys: Insights from nanoindentation

Francisco Javier Dominguez-Gutierrez[1]* (iD), Stefanos Papanikolaou[1] (iD),
Silvia Bonfanti[1] (iD), Mikko Alava[1,2] (iD)

[1] NOMATEN Centre of Excellence, National Center for Nuclear Research, 05-400 Świerk/Otwock, Poland.
[2] Department of Applied Physics, Aalto University, P.O. Box 11000, 00076 Aalto, Espoo, Finland.

Abstract

Deformation plasticity mechanisms in alloys and compounds may reveal the material's capacity towards optimal mechanical properties. We conducted a series of molecular dynamics (MD) simulations to investigate plasticity mechanisms due to nanoindentation in pure tungsten, molybdenum, and vanadium body-centered cubic single crystals, as well as the body-centered cubic, equiatomic, random solid solutions (RSS) of tungsten–molybdenum and tungsten–vanadium alloys. Our analysis focuses on a thorough, side-by-side comparison of dynamic deformation processes, defect nucleation, and evolution, along with corresponding stress–strain curves. We also checked the surface morphology of indented samples through atomic shear strain mapping. As expected, the presence of Mo and V atoms in W matrices introduces lattice strain and distortion, increasing material resistance to deformation and slowing down dislocation mobility of dislocation loops with a Burgers vector of $1/2 \langle 111 \rangle$. Our side-by-side comparison displays a remarkable suppression of the plastic zone size in equiatomic W–V RSS, but not in equiatomic W–Mo RSS alloys, displaying a clear prediction for optimal hardening response of equiatomic W–V RSS alloys. If the small-depth nanoindentation plastic response is indicative of overall mechanical performance, it is possible to conceive a novel MD-based pathway towards material design for mechanical applications in complex, multi-component alloys.

Keywords: nanoindentation, alloys, hardness, machine learning interatomic potentials, dislocation dynamics, plasticity, tungsten

1. Introduction

Tungsten–Molybdenum (W–Mo) alloys are promising materials with superior physical properties. These alloys are suitable for sustaining extreme operating conditions without degradation (Chen Q. et al., 2021; Kramynin, 2022; Lan et al., 2022; Liu et al., 2013; Sahoo et al., 2015). As the W percentage increases, the thermal conductivity decreases while the strength at both room and high temperatures increases (Chen Q. et al., 2020; Jiang et al., 2018; Ohser-Wiedemann et al.,

2013; Tao et al., 2022). In addition, Mo and W form isomorphic solid solutions due to their complete solid and liquid solubility, enabling the creation of solid solutions across the composition range (Gaffin et al., 2022; Lan et al., 2022; Wei et al., 2023). Nevertheless, it is known that tungsten exhibits relatively low fracture toughness at low temperatures, rendering it susceptible to cracking (Arshad et al., 2014; Gumbsch et al., 1998). As an alternative, the addition of vanadium to W matrices (W–V alloys) may enhance mechanical properties and improve creep resistance at elevated

temperatures (Jiang et al., 2019; Muzyk et al., 2011; Wei et al., 2023; Wurster et al., 2011). Furthermore, vanadium has recently been recognized as a unique element for strengthening in high entropy alloys and, more generically, random alloy solutions (Yin et al., 2020).

Nanoindentation simulations are capable of characterizing the mechanical response of materials under external loads at the nanoscale, particularly for their dislocation nucleation and evolution, as well as induced plastic patterning, referring to the creation of patterns or structures within the material (Domínguez-Gutiérrez et al., 2023; Varillas et al., 2017). It involves applying a small, sharp tip onto the material's surface, measuring the required force and the subsequent material displacement (Domínguez-Gutiérrez et al., 2021b; Kurpaska et al., 2022; Pathak & Kalidindi, 2015; Schuh, 2006; Varillas et al., 2017). This process finds various applications, such as developing nanostructured surfaces with enhanced functionalities and engineering materials with specific mechanical properties (Das et al., 2018; Li Z. et al., 2020). The plastic patterning resulting from nanoindentation is influenced by factors such as the applied load, material composition, and surface orientation. A deeper understanding of the material's deformation within the plastic zone beneath the indented surface region is essential for interpreting these effects (Mulewska et al., 2023a; Varillas et al., 2017; Wyszkowska et al., 2023).

In this work, we investigate the effects of vanadium in random solid solution W–based alloys, with a focus on the influence of varying vanadium concentrations on the morphology, densification, and mechanical properties, which have not been extensively studied in W-based alloys. (Wurster et al., 2011). Our aim is to gain insights into the behavior of alloys under external loads and explore the potential for developing novel material design methods. We achieve this by investigating nanoindentation-induced plasticity through load-displacement curves and surface patterning, as referenced in existing literature (Alcalá et al., 2012; Frydrych et al., 2023; Karimi et al., 2023; Oliver & Pharr, 1992; Schuh, 2006; Yu et al., 2020). Molecular dynamics (MD) simulations, particularly large-scale atomistic simulations, offer a cost-effective alternative for comprehending plastic deformation mechanisms in tungsten (W) and its alloys (Domínguez-Gutiérrez et al., 2021b, 2023; Kurpaska et al., 2022; Pitts et al., 2013; Varillas, 2019). The transition from elasticity to plasticity is characterized by pop-in events – sudden displacements indicating the initiation of dislocation sources in small indentation zones, as discussed in our work (Domínguez-Gutiérrez et al., 2023; Karimi et al., 2023; Pathak & Kalidindi, 2015; Pathak et al., 2014).

This phenomenon highlights a distinct drop in stress, a focal point in our study of equiatomic W–Mo and W–V alloys' hardening properties compared to single elements (Li T. L. et al., 2011; Mulewska et al., 2023b; Naghdi et al., 2022; Pöhl, 2019; Xiong et al., 2016), despite maintaining the body-centered cubic (BCC) crystalline structure.

2. Computational methods

We performed computer simulations using the Large-scale Atomic/Molecular Massively Parallel Simulator (LAMMPS) (Thompson et al., 2022) and the Embedded atom model with Finis–Sinclair (EAM-FS) potential developed for W–Mo and W–V by Chen Y. et al. (2020). This potential accurately models various physical and mechanical properties, $\langle 111 \rangle$ dumbbell migration, stacking fault energies, and relative stability of the $\langle 100 \rangle$ and $1/2\langle 111 \rangle$ interstitial dislocation loops. While, the surface energies of these two metals are reported to be slightly lower than the DFT results. Supplementary Material (SM), we report the elastic constants (C_{ij}), bulk modulus [GPa], shear modulus [GPa], Poisson's ratio, and the Young's modulus (E_Y [GPa]) of single element samples of W, Mo, and V, as well as random equatomic samples of W–Mo and W–V alloys that are generated by randomly substituting W atoms by Mo or V.

For modeling nanoindentation, the initial BCC samples of W, Mo, and V were created with lattice constants of approximately 0.316 nm, 0.315 nm, and 0.303 nm, respectively. The sample dimensions were deliberately selected to accommodate the expected dislocation loop propagation along slip families. For the [001] orientation, the dimensions, (d_x, d_y, d_z), were approximately 50 nm × 50.56 nm × 51.19 nm, encompassing 8,190,720 atoms. Similarly, for the [011] orientation, the sample was sized at around 50.24 nm × 51.84 nm × 49.16 nm, comprising 8,115,360 atoms. In the case of the [111] orientation, the sample measured approximately 51.40 nm × 50.09 nm × 50.63 nm, housing 8,424,900 atoms. The x and y axes have periodic boundary conditions to simulate an infinite surface, while the z orientation has a frozen bottom boundary to avoid vertical translation and to assure stability of the atoms when nanoindentation is performed, a thermostatic section above the frozen layer to dissipate the heat generated during nanoindentation, and a "dynamical" section for atoms–indenter interaction allowing atoms to move freely, as shown in Figure 1. Additionally, a 5 nm vacuum region is added atop the sample as an open boundary (Domínguez-Gutiérrez et al., 2021b; Kurpaska et al., 2022).

The W–Mo and W–V alloys are created by random substitution of 50% of W atoms from the initial BCC W sample with Mo or V atoms, as done previously, an assumption supported by thermodynamic binary alloy phase diagram calculations (Dominguez-Gutierrez et al., 2022; Muzyk et al., 2011; Turchi et al., 2005). The FIRE (fast inertial relaxation engine) 2.0 protocol (Guénolé et al., 2020) is then used to optimize the samples' geometry towards the closest local minimum of energy structure. We consider the following criteria for the optimization process where the change in energy between successive iterations and the most recent energy magnitude is less than 10^{-5} and when the global force vector length of all atoms is less than or equal to 10^{-8} eV/Å. We observed a 0.09% reduction in the cell volume of the W–Mo alloy after the optimization process, while the W–V alloy exhibited a substantial 7.77% decrease. Additionally, the d_z size of the W–V sample underwent a notable 9.73% reduction. These changes reflect the impact of V atoms on the W matrix. The samples are initially equilibrated at $T = 300$ K for 2 ns using an isobaric-isothermal ensemble. This equilibration is achieved by integrating the Nose–Hoover equations with damping parameters, specifically, $\tau_T = 2$ fs for the thermostat and $\tau_P = 5$ ps for the barostat, while maintaining an external pressure of 0 GPa (Kurpaska et al., 2022; Xu Q. et al., 2023). This process continues until the system attains homogeneous temperature and pressure profiles. In Figure 1, we illustrate the atomic distribution of W and Mo on the surface, underscoring the necessity of conducting multiple nanoindentation simulations to ensure robust statistical outcomes in our study.

The indenter tip is defined as a non-atomic repulsive imaginary (RI) rigid sphere, exerting a force of magnitude $F(t) = K(r(t) - R_i)^2$ on each atom. Here, $K = 236$ eV/Å^3 denotes the specified force constant, ensuring a high stiffness for our indenter tip (Varillas et al., 2017). The parameter $r(t)$ represents the distance from the atoms to the center of the indenter, and $R_i = 15$ nm is the radius of the indenter, chosen sufficiently large to accurately model the elastic-to-plastic deformation transition. Given that EAM potentials tend to yield lower surface energies than those obtained via DFT calculations, they lack the capability to simulate interactions between the indenter tip and the atoms on the top surface layer, particularly when the tip radius is equal to or less than 5 nm, as observed in our previous work computing normalized maximum shear stress by the pressure applied (Domínguez-Gutiérrez et al., 2023; Xu Q. et al., 2023). The initial location of the tip is set at a separation distance of 0.5 nm from the material's surface, and its center is randomly shifted to ten different positions to account for statistical variation, as depicted by black dots in Figure 1. We employ an NVE statistical thermodynamic ensemble with the velocity Verlet algorithm for an indenter speed of $v = 20$ m/s for 125 ps, using a time step of $\Delta t = 1$ fs. A maximum indentation depth of $h_{max} = 2.0$ nm is selected to minimize boundary layer effects in the dynamic atoms region.
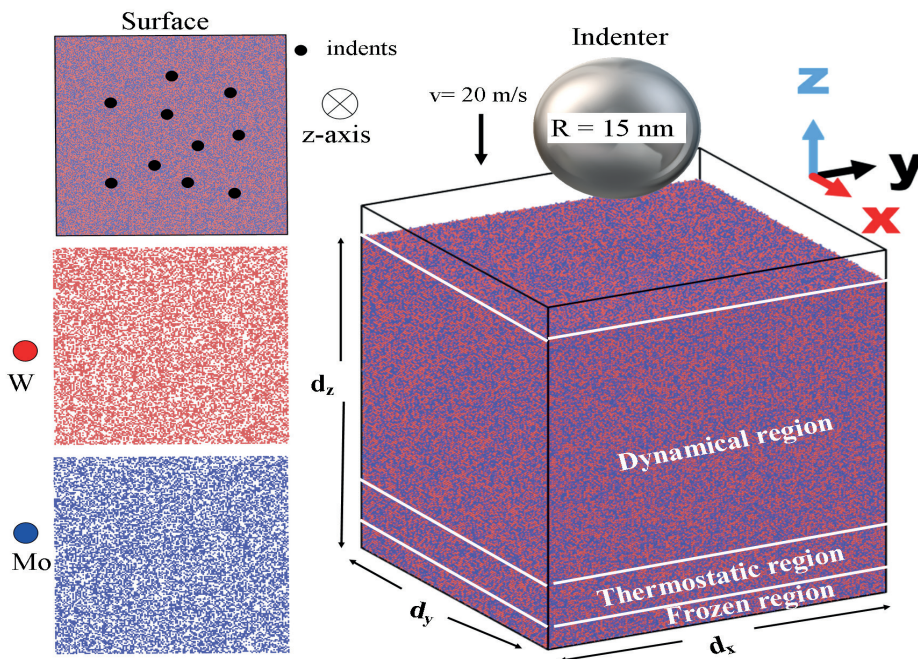

Fig. 1. Standard setup employed in our MD simulations for nanoindentation. The samples are partitioned into three regions to account for boundary conditions. We employ a non-atomic repulsive spherical indenter at a given strain rate. The target area configuration displays the random atomic distribution within the sample with black dots as indenter marks

3. Results

The common pathway to investigate nanoindentation is through average force-displacement curves, which gives the information to define the mean contact pressure p as (Johnson, 1987; Remington et al., 2014; Varillas, 2019):

$$p(h) = \frac{2\pi}{3E_Y} \left[24 P_{ave}(h) \left(\frac{E_Y R_i}{1-v^2} \right)^2 \right]^{1/3} \qquad (1)$$

where h is the indentation depth, v is the Poisson's ratio, and the average load is calculated as $P_{ave}(h) = 1/N \sum_i^N P_i(h)$ with $P_i(h)$ as the load from each MD simulation and $N = 10$ the number of indents. During loading process, the contact radius is obtained with the geometrical relationship (Domínguez-Gutiérrez et al., 2023):

$$a(h) = \left[3 P_{ave}(h) R_i \frac{1-v^2}{8E_Y} \right]^{1/3} \qquad (2)$$

Quantities $p(h)$ and $a(h)$ provide an intrinsic measure of the surface resistance to defect nucleation (Domínguez-Gutiérrez et al., 2023; Varillas et al., 2017) and yield to a universal linear relationship between $p(h)/E_Y$ and $a(h)/R_i$ given by:

$$\frac{p(h)}{E_Y} = \frac{0.844}{1-v^2} \frac{a(h)}{R_i} \qquad (3)$$

Figures 2 and 3 show the ratio between $p(h)$ and the Young's modulus E_Y, for each sample, as a function of the normalized contact radius $a(h)/R_i$ between the sample and the tip. This is utilized to identify the pop-in event, where the contact pressure deviates from the linear geometric fitting showing plastic instability initiated as a notable pressure drop.

To assess the advantages and limitations of our approach, we conducted a comparative analysis, contrasting our findings with those derived from a machine-learned interatomic potentials (MLIP) based on the tabulated Gaussian approximation potential framework (tabGAP) (Byggmästar et al., 2021). The tabGAP employs the EAM-FS potentials within the training dataset, incorporating concise low-dimensional descriptors, including two-body, three-body, and an EAM-like density. In addition, the utilization of the low-dimensional descriptors facilitates the creation of more efficient tabulated versions, where MLIP energy contributions are mapped onto grids (Byggmästar et al., 2021). In Figures 2 and 3, we observed a reasonable correspondence in characterizing the transition from elastic to plastic deformation using both EAM-FS and tabGAP.

However, it's important to note a distinct occurrence of the pop–in event, which falls within a range of 0.01 to 0.05 p/E_Y. This discrepancy may be attributed to the incorporation of additional surface energy information within the tabGAP framework. Additionally, our findings were compared to our prior results for Mo (Domínguez-Gutiérrez et al., 2021a, 2021b), where the use of EAM potentials with short interatomic distances corrections by the repulsive Ziegler–Biersack–Littmark (ZBL) model (Salonen et al., 2003) exhibited a higher contact pressure value at the pop-in event.
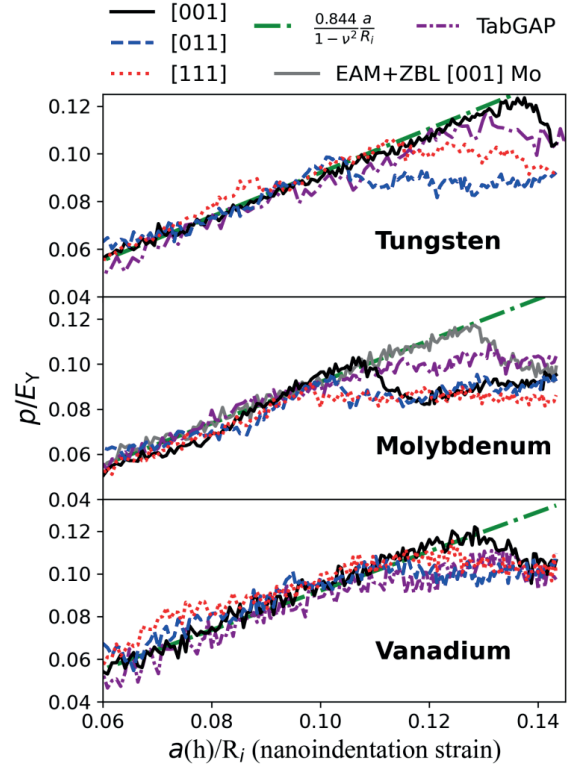

Fig. 2. Contact pressure evolution p, normalized by Young's modulus E_Y is depicted with normalized contact radius $a(h)/R_i$ for W, Mo, and V matrices. The figure employs the following color scheme: a solid black line for [001] orientation, a dashed blue line for [011], and a dotted red line for [111]. The results conform to the universal linear relationship $[0.844/(1-v^2)]$ $[a(h)/R_i]$, illustrated with the green dashed-dotted line. To validate our findings, comparisons with tabGAP (Byggmästar et al., 2021; Domínguez-Gutiérrez et al., 2023) for [001] samples are depicted with purple double dotted-dashed lines, and for the [001] Mo sample with EAM+ZBL simulations (Domínguez-Gutiérrez et al., 2021b; Salonen et al., 2003) represented by gray solid lines

From our MD simulations, the [001] orientation displayed the highest critical load, suggesting enhanced resistance to plastic deformation. Transitioning to the effects on Mo–W and M–V alloys, Figure 3 demonstrates the influence of Mo and V atoms in the

W matrix. For Mo, the maximum value of $p(h)/E_Y$ at [001] orientation is at 0.12 $a(h)/R_i$, between those of pure W and Mo, consistent across orientations. Also, the pressure drop is more pronounced for [001]W–Mo compared to pure W and Mo. Conversely, V atoms in W lead to decreased yield points across orientations, in agreement with the V sample but distinct from W matrices. Notably, the max($p(h)/E_Y$) for [001]W–V is 0.11 $a(h)/R_i$, lower than in pure W and V, signifying the onset of exceptional work hardening.
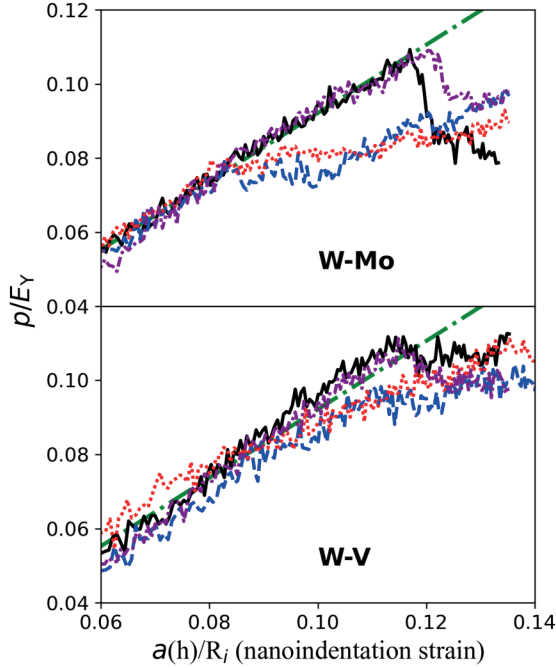

Fig. 3. Average contact pressure evolution as a function of the contact area for W–Mo and W–V alloys. TabGAP simulation results are depicted for the [001] orientation, in good agreement with EAM-FS outcomes. The color scheme is similar to the one shown in Figure 2

In our prior study (Domínguez-Gutiérrez et al., 2023), we approximated the onset of dislocation nucleation with ∼0.45 – 0.5$h/a(h)$. Therefore, to estimate the maximum shear stress using contact pressure calculations, we assume an isotropic Hertzian contact model (Li T. L. et al., 2011). The maximum shear stress beneath the indenter tip (τ_{Max}) is computed as $\tau_{max} = 0.465\max(p(h))$, where $p(h)$ is the contact pressure obtained from Figures 2 and 3 (Li T. L. et al., 2011; Xiong et al., 2016). The obtained maximum shear stress under the indenter tip for single elements (W, Mo, V) and binary alloys (W–Mo, W–V) for the [001] orientation is shown in Table 1, with EAM-FS and tabGAP results in normal and bold respectively. We used the shear modulus (G) computed using the EAM-FS potentials at 300 K to determine the maximum shear stress.

Table 1. Maximum shear stress, $\tau_{max} = 0.465\max(p_m)$ (Li T. L. et al., 2011), under the indenter tip for single elements (W, Mo, V) and binary alloys (W–Mo, W–V) on the [001] crystal orientation for a strain rate of 20 m/s and 5 m/s. Additionally, the theoretical shear stress ($\tau_{theor} = G/(2\pi)$) is provided, where G represents the shear modulus

	W	Mo	V	W–Mo	W–V
EAM-FS	**22.50**	**18.75**	**7.52**	**19.71**	**12.68**
TabGAP	21.61	19.20	7.06	20.06	12.02
G	136	122	43	135	84
Theor.	21.65	19.45	6.84	21.56	13.37

3.1. Dislocation network analysis

In general, dislocation glide predominantly occurs along the closest-packed ⟨111⟩ directions for BCC metals, where the Burgers vector is denoted as $b = 1/2\langle111\rangle$. The associated slip planes are typically {110} and {112}. To analyze the atomic structure during nanoindentation tests, which provide insights into the mechanisms of dislocation nucleation and evolution (Domínguez-Gutiérrez et al., 2023), we employ OVITO (Stukowski, 2010) along with the DXA package (Stukowski et al., 2012). This approach allows us to identify dislocations, categorizing them into distinct types based on their Burgers vectors, such as the $1/2\langle111\rangle$, ⟨100⟩, and ⟨110⟩ dislocation types. Figure 4 shows material dislocations of selected MD simulation at maximum indentation depth for the [111] orientation, determined by the DXA method. Single-element matrices form a single dislocation loop on the {111} slip plane, along with an embryonic dislocation (Burgers vector $1/2\langle1\bar{1}1\rangle$) traveling the {112} plane. Mo initiates a single dislocation loop and creates an embryonic dislocation on the {112} plane with the same Burgers vector. V matrices exhibit shear loop formation under the indenter, indicating plasticity. However, embryonic dislocation movement is limited, favoring lateral motion instead. This leads to a dislocation loop (Burgers vector $1/2\langle\bar{1}\bar{1}1\rangle$) followed by a second loop, typical in BCC materials (Alcalá et al., 2012).

We present results for [001] and [011] orientations in Supplementary Material of this paper, for single element materials at [001] orientation (tungsten at Fig. 4), two dislocation loops propagate within the Mo matrix, with Burgers vectors of $1/2\langle111\rangle$ and symmetrical ones of $1/2\langle1\bar{1}1\rangle$. In contrast, W and V samples exhibit shear loops developing toward {111} slip planes. This consistency aligns with Figure 2, where Mo maintains consistent p/E_Y values beyond 0.1$a(h)/R_i$, while others experience a contact pressure drop. For [110] orientation, W, Mo, and V matrices exhibit lasso-like mechanisms,

with screw dislocations evolving Burgers vectors of $1/2\langle 1\bar{1}\bar{1}\rangle$ and $1/2\langle 111\rangle$, forming dislocation loops. W forms perfect loops, while Mo and V generate distorted ones due to material specific mechanical properties and Peierls barrier effects (Grigorev et al., 2023).
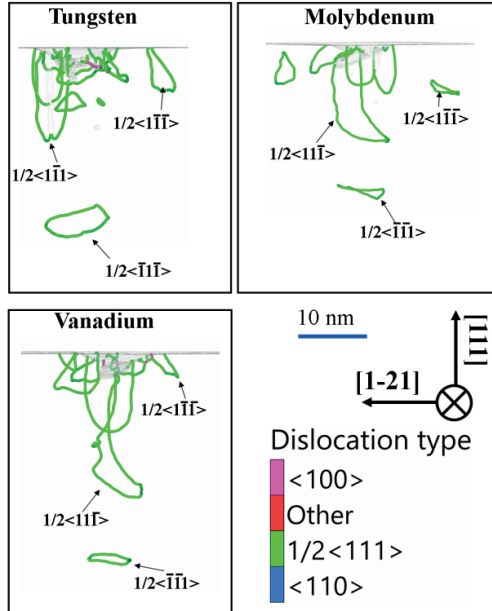

Fig. 4. Visualization of dislocations nucleated and evolved at the maximum indentation depth of 2 nm for single-element tungsten (W), molybdenum (Mo), and vanadium (V) samples on the [111] orientation. A dislocation loop with a Burgers vector of $1/2\langle 111\rangle$ is observed for all the samples

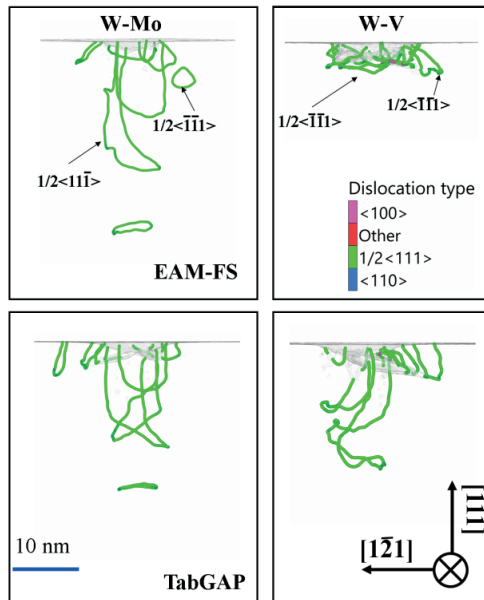**Fig. 5.** Dislocation networks at the maximum indentation depth of 2 nm are portrayed for the W–Mo and W–V in alloys using EAM-FS and tabGAP approaches. A discrepancy is noticeable in the nucleation of dislocations in both approaches, stemming from the inclusion of a comprehensive training dataset for the MLIP that incorporates sufficient surface energy information

In Figure 5, the results for W–Mo and W–V alloys indicate the presence of screw dislocations, showcasing distinctive half loops encircling the indenter tip location. For W–Mo, two dislocation loops originate, while in the 50% V atoms alloy with W, screw dislocation propagation on the {111} plane notably diminishes during EAM-FS simulations. Although the MD simulations for pristine cases align with those reported by tabGAP (Domínguez-Gutiérrez et al., 2023), discrepancies arise in the W–Mo and W–V alloy analyses. While tabGAP identifies an edge dislocation loop for W–Mo, the dislocation dynamics and nucleation differ significantly in the W–V alloy. Notably, V in W matrices triggers wave-wise dislocations underneath the tip due to lattice mismatch, leading to the initiation of a loop. This variance between EAM-FS and tabGAP is due to differences in their training data, supported by DFT calculations of Peierls barrier energies (Byggmästar et al., 2022). Results for [001] and [011] orientations are depicted in the Supplementary Material.

3.2. Indented surfaces analysis

During nanoindentation loading, the indenter tip forms pile-ups and slip traces around it (Kurpaska et al., 2022; Pathak & Kalidindi, 2015), offering insight into dislocation propagation (Yu et al., 2020). To explore this, we calculate the strain tensor at maximum indentation depth using the elastic Eulerian-Almansi finite strain tensor (Stukowski et al., 2012) that describes local elastic deformation. Figure 6 displays strain field maps for [011] orientation of W in good agreement with experimental results given by Yu et al. (2020), aligning high-resolution EBSD data. Positive max strain (ϵ_{xx}) concentrates under the indenter, negative strain appears between {112} planes. ϵ_{xy} displays four-fold symmetry, ϵ_{xz} and ϵ_{yz} exhibit positive and negative poles aligned with {110} family planes, as shown by the Kikuchi wise pattern (Yu et al., 2020). In SM, we report that Mo and V exhibit similar strain patterns but with differing magnitudes due to lattice parameters and elasticity. V emphasizes strain accumulation around {110} and {112} planes in ϵ_{xx} and ϵ_{yy}. These strain maps unveil localized deformation patterns and crystallographic strain dependence in the studied materials.

In Figure 7, we illustrate strain distribution for [111] W–V alloy by EAM-FS and tabGAP. W–Mo alloy exhibits notable strain accumulation beneath the indenter tip along the {110} plane, largely in $\epsilon_{xx,yz}$ for EAM-FS, while the tabGAP simulations show maximum values of strain on the direction of the dislocation nucleated by the applied stress.
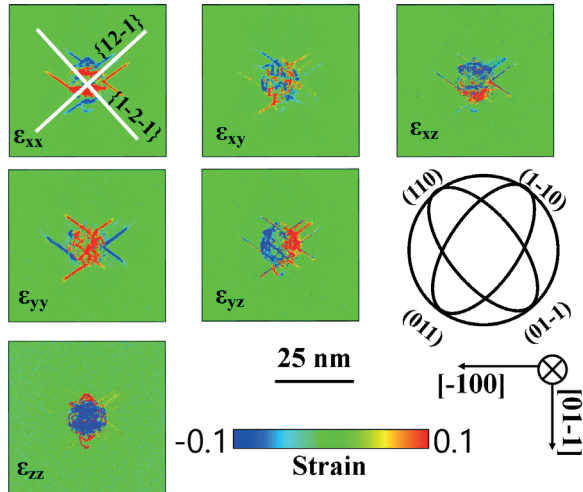
Fig. 6. Strain field mapping around the indenter tip at the maximum depth for [101]W noticing a good qualitative agreement with experimental results reported by Yu et al. (2020) and Das et al. (2018) following {112} plane families and Kikuchi wise pattern with (011) directions
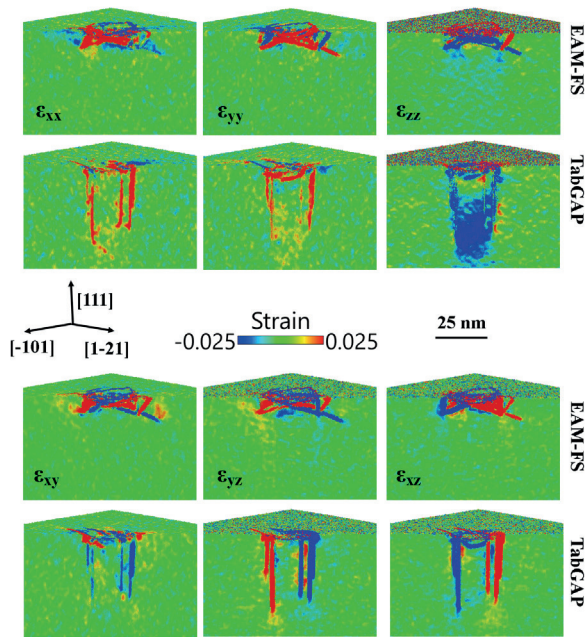

Fig. 7. Strain field mapping at the maximum indentation depth for the [101]W–V alloy using both EAM–FS and tabGAP potentials showing the difference in modeling nanomechanical during the loading process. While both approaches exhibit agreement in global calculations related to maximum shear stress, they diverge in modeling the evolution of dislocations in the W–V alloy. This difference is attributed to the more robust training data set of the tabGAP compared to the traditional EAM method, influencing their modeling of dislocation dynamics within the alloy

This arises due to V's presence in the W matrix, influencing strain and causing dislocation buildup under the tip. The strain mapping depicts dislocation evolution in

this direction. In addition, strain mapping of the [111] W–V alloy indicates localized positive and negative strains under the tip, represented by $\epsilon_{xy,yz,zy}$, without significant strain propagation along crystallographic planes, as observed in tabGAP simulations. This observation suggests limited dislocation propagation within the alloy, a pattern that aligns with the representations in Figure 4. These outcomes emphasize the limitations of EAM-FS in depicting dislocation propagation, despite its strong agreement with strain-stress curves and maximum shear stress values from tabGAP. In the SM, we depict the strain mapping of the W–Mo alloy, revealing a reasonable agreement between both approaches. Understanding the distribution of strain and its dependence on crystallography is of importance for comprehending the mechanical response and deformation mechanisms present in these binary alloys.

3.3. Nanoindentation strain rate analysis

It appears that simulations conducted using the EAM-FS potential showcase good alignment with the more sophisticated MLIP methods, save for a noticeable difference in dislocation nucleation, particularly observed in the W–V alloy. However, it's important to note a substantial difference in computational wall time between these approaches. While an MD simulation using the EAM method within our computational setup, employing 120 processors, can be completed in a matter of hours, a tabGAP simulation requires several days to run due to this significant disadvantage. Consequently, to address this drawback of the tabGAP method, we opted to conduct MD simulations at a nanoindentation strain rate of 5 m/s using the EAM-FS potentials while maintaining the same numerical setup utilized for the 20 m/s case. Our primary aim is to explore the influence of strain rate on the maximum shear stress of the samples, where the EAM method exhibits strong agreement with tabGAP, except in dislocation nucleation.

Figure 8 present the results for the average contact pressure, $p_m = P_{ave}/\pi a(h)$, at a nanoindentation rate of $v = 5$ m/s for the single–element samples W, Mo, and V, as well as the binary alloys W–Mo and W–V for the [001] orientation, respectively (Alcalá & Esqué-de los Ojos, 2010). We observed a sudden drop in the critical contact pressure, akin to what's observed in compression mechanical tests (Papanikolaou et al., 2012, 2017; Song et al., 2019a, 2019b; Xu R.-G. et al., 2021), linked to the pop-in event during loading. Furthermore, the maximum value of p_m, signifying the initiation of plastic deformation, varied among materials. In MD simulations, the sequence of the p_m values is W, Mo,

and V indicating that tungsten (W) demonstrated the highest resistance to plastic deformation. Additionally, the contact pressure decreases with decreasing nanoindentation strain rate, primarily observed in the binary alloys, consistent with experimental findings (Huo et al., 2019). This effect is due to the slower indenter tip penetration, allowing more time for dislocation evolution within the sample and shock absorption between the tip and the surface. In W–Mo alloys, the maximum value of p_m falls between that of Mo and W for both the [011] and [001] orientations, as expected. In W–V alloys, regardless of crystal orientation, this value falls between that of V and W.
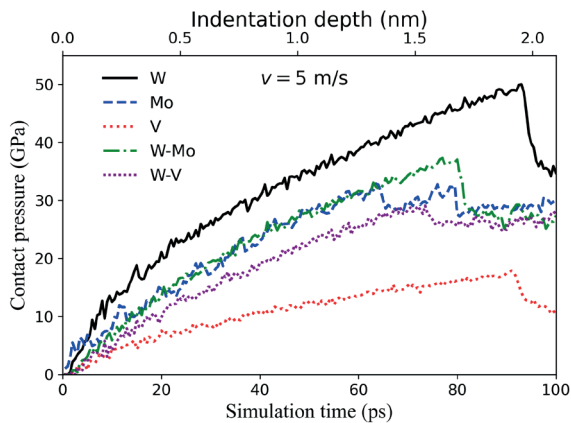

Fig. 8. The evolution of contact pressure is presented as a function of the simulation time and depth at a nanoindentation strain rate of 5 m/s for single-element W, Mo, and V matrices, and W–Mo and W–V alloys oriented along [001]. The contact pressure is averaged across 10 MD simulations for each sample, illustrating the transition from the elastic to the plastic deformation region

Table 2. Maximum shear stress, $\tau_{max} = 0.465 \max(p_m)$ (Li T. L. et al., 2011), under the indenter tip for single elements (W, Mo, V) and binary alloys (W–Mo, W–V) at different crystal orientations ([001], [011], [111]) for a strain rate of 5 m/s. Additionally, the theoretical shear stress ($\tau_{theor} = G/(2\pi)$) is provided, where G represents the shear modulus

	W	Mo	V	W–Mo	W–V
[001]	22.95	18.53	8.01	20.34	12.18
[011]	17.32	16.63	6.09	14.86	13.51
[111]	18.55	16.83	6.98	14.53	–
G	136	122	43	135	84
Theor.	21.65	19.45	6.84	21.56	13.37

In Table 2 we report results for the maximum shear stress for 5 indenter speed. We noticed that the crystallographic orientation significantly influences both the contact pressure yield point and maximum shear stress values. The τ_{Max} beneath the indenter tip is in the order of the τ_{theor} for the [001] orientations across all samples.

Furthermore, the W–V alloy displayed heightened ductility for the [111] crystal orientation. This was evident in the contact pressure analysis, where the indenter tip needed to penetrate deeper into the sample to reach the yield point. Results at a rate of 20 m/s are presented in the SM.

3.4. Generalized stacking fault energies

We compute Generalized Stacking Fault Energy (GSFE) curves by considering two distinct lattice orientations that align the x–z plane with the targeted glide plane. To define the samples, we take a unit cell with lattice vectors as $\langle 112 \rangle_x$, $\langle 110 \rangle_y$, and $\langle 111 \rangle_z$ for the {110} plane case, and $\langle 110 \rangle_x$, $\langle 112 \rangle_y$, and $\langle 111 \rangle_z$ for the {112} plane case. These unit cells are then replicated in a $12 \times 10 \times 5$ supercell, defining 3600 atoms with a 2.0 nm vacuum introduced at one end in the y direction to prevent interactions between periodic images (Wang et al., 2021; Xu S. et al., 2020).

The computation of each GSFE curve involves displacing the top half layers of atoms relative to the bottom half in the $\langle 111 \rangle_z$ direction. Displacements occur at equal increments, with each increment representing a fraction of 0.1 of the Burgers vector magnitude. After each displacement, the top and bottom atomic layers are held fixed, while the remaining layers undergo relaxation solely in the y direction. The relaxation process, achieved through energy minimization using the conjugate gradient scheme, concludes when either (i) the quotient of the change in energy between successive iterations and the most recent energy magnitude is less than 10^{-12} or (ii) when the global force vector length of all atoms is less than or equal to 10^{-12} eV/Å (Wang et al., 2021). Then, the stacking fault energy can be calculated as (Ojha et al., 2014):

$$\gamma_{GSFE} = \frac{E_s - E_0}{A_{SF}} \tag{4}$$

where E_s represents the energy of the sample at a given displacement, and E_0 denotes the energy for the perfect sample, A_{SF} stands for the stacking fault area.

In Figure 9, the results for γ_{GSFE} on the {110} and {112} planes for pure W, Mo, and V are presented. These findings are juxtaposed with DFT calculations for W and Mo (Wang et al., 2021), and V (Zhang et al., 2017), as well as with the machine learning potential SNAP for W and Mo (Wang et al., 2021). Additionally, results for Mo using EAM+ZBL potentials (Salonen et al., 2003) are included. Notably, a commendable agreement is observed between tabGAP and DFT results for W and Mo, notwithstanding a slight discrepancy with V in the {112} plane. Regarding the EMA–FS

results, it is noteworthy that the γ_{GSFE} curves are lower than those obtained through DFT, impacting the modeling of defect nucleation during the loading process.
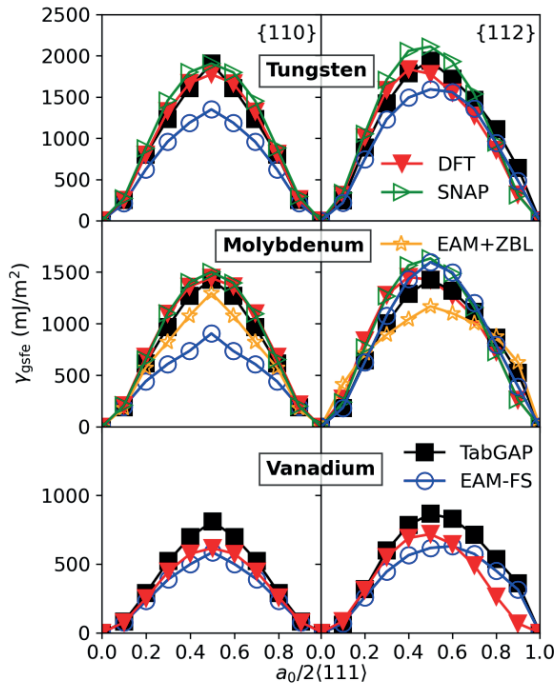

Fig. 9. Relaxed γ_{GSFE} curves on the {110} and {112} planes for pure W, Mo, and V. The presented results are compared to DFT calculations for W and Mo (Wang et al., 2021) and V (Zhang et al., 2017), as well as to other machine learning potential SNAP for W and Mo (Wang et al., 2021). Additionally, results for Mo using EAM+ZBL potentials (Salonen et al., 2003) are included. Notably, a good agreement is observed between tabGAP and DFT results
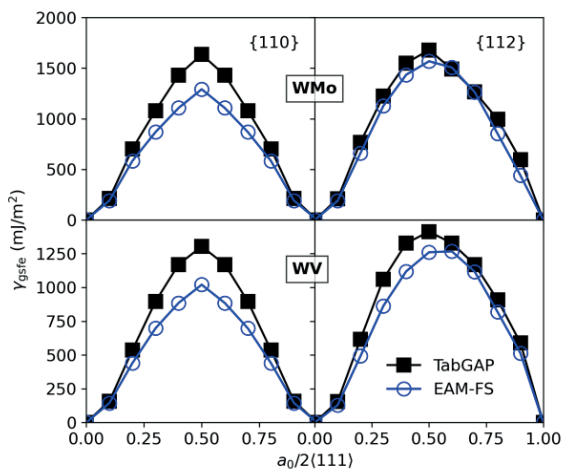

Fig. 10. Relaxed γ_{GSFE} curves are presented for the {110} plane and the {112} plane for W–Mo and W–V alloys using EAM-FS and tabGAP potentials. It is noteworthy that the energy values are consistently lower for EAM-FS compared to tabGAP, providing an explanation for the observed difference in dislocation nucleation during nanoindentation loading

In Figure 10, results for γ_{GSFE} curves for the binary alloys WMo and WV are depicted using EAM-FS and tabGAP methods. Generally, the energy values for tabGAP are higher than those presented by the EAM-FS method, particularly noticeable for the {110} plane. Notably, in the case of the W–V alloy, there is a substantial difference in energies between the two methods, especially for the {112} plane. This difference may elucidate the observed discrepancy in the nucleation of the dislocation network during the load process for the [111] W–V alloy. Specifically, the EAM-FS method requires a higher pressure for the propagation of dislocations.

4. Concluding remarks

Understanding the mechanical behavior in W-based random solution alloys is important for applications at extreme operating conditions. Our molecular dynamics simulations delved into nanoindentation responses within pure tungsten, molybdenum, vanadium, and their equiatomic W–Mo and W–V random solid solution alloys. Our analysis compared dynamic deformation, defect formation, stress-strain behaviors, and surface morphologies post-indentation. We conducted simulations employing the EAM method and explored its limitations by contrasting it with a more sophisticated, machine-learned interatomic potential within the Gaussian approximation potential (GAP) framework. These interatomic potentials are reported in the NIST database and, according to the authors' knowledge, are the only ones currently developed suitable for performing open-boundary molecular dynamics (MD) simulations for W–Mo and W–V alloys. The introduction of Mo and V into W structures reduces the Generalized Stacking Fault Energy (GSFE) values, consequently decreasing the dislocation mobility. Intriguingly, equiatomic W–V alloys displayed significant suppression of the plastic zone, indicating enhanced hardening potential compared to W-Mo counterparts. In the case of the former, we observed disparities between the EAM approach and tabGAP. EAM encountered limitations in modeling dislocation nucleation and evolution, particularly in the [111] crystal orientation. Conversely, tabGAP predicted the formation of shear loops and slower dislocation evolution. EAM indicated concentrated strain beneath the indenter tip, forming a dislocation network without effective propagation, possibly due to lower surface energies when compared to DFT calculations. Nevertheless, maximum shear stress values obtained with the EAM method are in good agreement with the theoretical results showing a crystallographic dependence for all the materials. The computed generalized stacking fault energy curves for tabGAP demonstrate a commendable

agreement with ab initio calculations, particularly for the {110} plane. Additionally, they provide insights into asymmetry concerning the sense of glide direction on the {112} plane, a crucial factor contributing to the observed differences in dislocation nucleation modeling in binary alloys. Our findings suggest a promising avenue for computational material design in complex, multi-component alloys, emphasizing insights gained from small-depth nanoindentation responses.
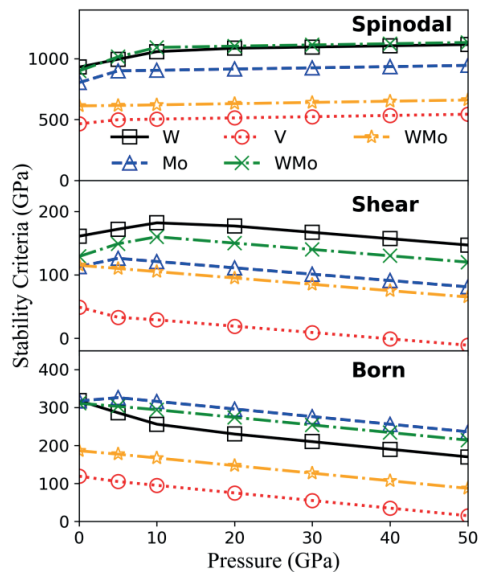

Fig. 11. Spinodal, shear, and Born stability criteria with hydrostatic pressure for single W, Mo, V, and binary alloy WMo and WV. The pressure range showing the stability of the interatomic potentials is considered to set up the numerical conditions in the MD simulations

Appendix A:
Elastic stability of interatomic potentials

To validate the suitability of the EAM-FS potentials for simulations under high-stress conditions, we assess the elastic constants within a pressure range relevant to the loading process (Xiong et al., 2016). We further examine the elastic stability conditions by evaluating the spinodal, shear, and Born criteria (Xiong et al., 2014) under hydrostatic pressure P. These criteria, denoted as M1 = C_{11} + 2C_{12} + P > 0, M2 = C_{44} − P > 0, and M3 = C_{11} − C_{12} − 2P > 0, are shown in Figure 11. Notably, the materials exhibit stability from 0 GPa to 50 GPa, which is taken into account to set up the numerical environment for nanoindentation simulations.

Acknowledgements

References

Alcalá, J., & Esqué-de los Ojos, D. (2010). Reassessing spherical indentation: Contact regimes and mechanical property extractions. *International Journal of Solids and Structures*, *47*(20), 2714–2732. https://doi.org/10.1016/j.ijsolstr.2010.05.025.

Alcalá, J., Dalmau, R., Franke, O., Biener, M., Biener, J., & Hodge, A. (2012). Planar defect nucleation and annihilation mechanisms in nanocontact plasticity of metal surfaces. *Physical Review Letters*, *109*, 075502. https://doi.org/10.1103/PhysRevLett.109.075502.

Arshad, K., Zhao, M.-Y., Yuan, Y., Zhang, Y., Zhao, Z.-H., Wang, B., Zhou, Z.-J., & Lu, G.-H. (2014). Effects of vanadium concentration on the densification, microstructures and mechanical properties of tungsten vanadium alloys. *Journal of Nuclear Materials*, *455*(1–3), 96–100. https://doi.org/10.1016/j.jnucmat.2014.04.019.

Byggmästar, J., Nordlund, K., & Djurabekova, F. (2021). Modeling refractory high-entropy alloys with efficient machine-learned interatomic potentials: Defects and segregation. *Physical Review B*, *104*(10), 104101. https://doi.org/10.1103/PhysRevB.104.104101.

Byggmästar, J., Nordlund, K., & Djurabekova, F. (2022). Simple machine-learned interatomic potentials for complex alloys. *Physical Review Materials*, *6*(8), 083801. https://doi.org/10.1103/PhysRevMaterials.6.083801.

Chen, Q., Liang, S., Zhang, J., Zhang, X., Wang, Ch., Song, X., & Zhuo, L. (2020). Preparation and characterization of WMo solid solution nanopowders with a wide composition range. *Journal of Alloys and Compounds*, *823*, 153760. https://doi.org/10.1016/j.jallcom.2020.153760.

Chen, Q., Liang, S., Li, B., Chen, Z., Song, X., & Zhuo, L. (2021). Sol-gel synthesis and characterization of tungsten-molybdenum solid solution nanoparticles. *International Journal of Refractory Metals and Hard Materials*, *100*, 105668. https://doi.org/10.1016/j.ijrmhm.2021.105668.

Chen, Y., Liao, X., Gao, N., Hu, W., Gao, F., & Deng, H. (2020). Interatomic potentials of W–V and W–Mo binary systems for point defects studies. *Journal of Nuclear Materials*, *531*, 152020. https://doi.org/10.1016/j.jnucmat.2020.152020.

Das, S., Armstrong, D. E. J., Zayachuk, Y., Liu, W., Xu, R., & Hofmann, F. (2018). The effect of helium implantation on the deformation behaviour of tungsten: X-ray micro-diffraction and nanoindentation. *Scripta Materialia*, *146*, 335–339. https://doi.org/10.1016/j.scriptamat.2017.12.014.

Domínguez-Gutiérrez, F. J., Byggmästar, J., Nordlund, K., Djurabekova, F., & Toussaint, U., von (2021a). Computational study of crystal defect formation in Mo by a machine learning molecular dynamics potential. *Modelling and Simulation in Materials Science and Engineering*, *29*(5), 055001. https://doi.org/10.1088/1361-651X/abf152.

Domínguez-Gutiérrez, F. J., Papanikolaou, S., Esfandiarpour, A., Sobkowicz, P., & Alava, M. (2021b). Nanoindentation of single crystalline Mo: Atomistic defect nucleation and thermomechanical stability. *Materials Science and Engineering: A*, *826*, 141912. https://doi.org/10.1016/j.msea.2021.141912.

Dominguez-Gutierrez, F. J., Ustrzycka, A., Xu, Q. Q., Alvarez-Donado, R., Papanikolaou, S., & Alava, M. J. (2022). Dislocation nucleation mechanisms during nanoindentation of concentrated FeNiCr alloys: unveiling the effects of Cr through molecular simulations. *Modelling and Simulation in Materials Science and Engineering*, *30*(8), 085010. https://doi.org/10.1088/1361-651X/ac9d54.

Domínguez-Gutiérrez, F. J., Grigorev, P., Naghdi, A., Byggmästar, J., Wei, G. Y., Swinburne, T. D., Papanikolaou, S., & Alava, M. J. (2023). Nanoindentation of tungsten: From interatomic potentials to dislocation plasticity mechanisms. *Physical Review Materials*, *7*, 043603. https://doi.org/10.1103/PhysRevMaterials.7.043603.

Frydrych, K., Dominguez-Gutierrez, F. J., Alava, M. J., & Papanikolaou, S. (2023). Multiscale nanoindentation modelling of concentrated solid solutions: A continuum plasticity model. *Mechanics of Materials*, *181*, 104644. https://doi.org/10.1016/j.mechmat.2023.104644.

Gaffin, N. D., Ang, C., Milner, J. L., Palomares, K. B., & Zinkle, S. J. (2022). Consolidation behavior of Mo30W alloy using spark plasma sintering. *International Journal of Refractory Metals and Hard Materials*, *104*, 105778. https://doi.org/10.1016/j.ijrmhm.2022.105778.

Grigorev, P., Goryaeva, A. M., Marinica, M.-C., Kermode, J. R., & Swinburne, T. D. (2023). Calculation of dislocation binding to helium-vacancy defects in tungsten using hybrid ab initio-machine learning methods. *Acta Materialia*, *247*, 118734. https://doi.org/10.1016/j.actamat.2023.118734.

Guénolé, J., Nöhring, W. G., Vaid, A., Houllé, F., Xie, Z., Prakash, A., & Bitzek, E. (2020). Assessment and optimization of the fast inertial relaxation engine (FIRE) for energy minimization in atomistic simulations and its implementation in LAMMPS. *Computational Materials Science*, *175*, 109584. https://doi.org/10.1016/j.commatsci.2020.109584.

Gumbsch, P., Riedle, J., Hartmaier, A., & Fischmeister, H. F. (1998). Controlling factors for the brittle-to-ductile transition in tungsten single crystals. *Science*, *282*(5392), 1293–1295. https://doi.org/10.1126/science.282.5392.1293.

Huo, W., Fang, F., Liu, X., Tan, S., Xie, Z., & Jiang, J. (2019). Remarkable strain-rate sensitivity of nanotwinned CoCrFeNi alloys. *Applied Physics Letters*, *114*(10), 101904. https://doi.org/10.1063/1.5088921.

Jiang, D., Zhou, Q., Xue, L., Wang, T., & Hu, J. (2018). First-principles study the phase stability and mechanical properties of binary W-Mo alloys. *Fusion Engineering and Design*, *130*, 56–61. https://doi.org/10.1016/j.fusengdes.2018.03.050.

Jiang, D., Zhou, Q., Liu, W., Wang, T., & Hu, J. (2019). First-principles study the structures and mechanical properties of binary W-V alloys. *Physica B: Condensed Matter*, *552*, 165–169. https://doi.org/10.1016/j.physb.2018.10.005.

Johnson, K. L. (1987). *Contact Mechanics*. Cambridge University Press.

Karimi, K., Salmenjoki, H., Mulewska, K., Kurpaska, L., Kosińska, A., Alava, M. J., & Papanikolaou, S. (2023). Prediction of steel nanohardness by using graph neural networks on surface polycrystallinity maps. *Scripta Materialia*, *234*, 115559. https://doi.org/10.1016/j.scriptamat.2023.115559.

Kramynin, S. P. (2022). Theoretical study of concentration and size dependencies of the properties of Mo–W alloy. *Solid State Sciences*, *124*, 106814. https://doi.org/10.1016/j.solidstatesciences.2022.106814.

Kurpaska, L., Dominguez-Gutierrez, F. J., Zhang, Y., Mulewska, K., Bei, H., Weber, W. J., Kosińska, A., Chrominski, W., Jozwik, I., Alvarez-Donado, R., Papanikolaou, S., Jagielski, J., & Alava, M. (2022). Effects of Fe atoms on hardening of a nickel matrix: Nanoindentation experiments and atom-scale numerical modeling. *Materials & Design*, *217*, 110639. https://doi.org/10.1016/j.matdes.2022.110639.

Lan, X., Zhang, H., Li, Z.-B., & Zhang, G.-H. (2022). Preparation of fine-grained MoW solid solution alloys with excellent performances. *Materials Characterization*, *191*, 112140. https://doi.org/10.1016/j.matchar.2022.112140.

Li, T. L., Gao, Y. F., Bei, H., & George, E. P. (2011). Indentation Schmid factor and orientation dependence of nanoindentation pop-in behavior of NiAl single crystals. *Journal of the Mechanics and Physics of Solids*, *59*(6), 1147–1162. https://doi.org/10.1016/j.jmps.2011.04.003.

Li, Z., Gao, S., Brand, U., Hiller, K., & Wolff, H. (2020). A MEMS nanoindenter with an integrated AFM cantilever gripper for nanomechanical characterization of compliant materials. *Nanotechnology*, *31*(30), 305502. https://doi.org/10.1088/1361-6528/ab88ed.

Liu, G., Zhang, G. J., Jiang, F., Ding, X. D., Sun, Y. J., Sun, J., & Ma, E. (2013). Nanostructured high-strength molybdenum alloys with unprecedented tensile ductility. *Nature Materials*, *12*(4), 344–350. https://doi.org/10.1038/nmat3544.

Mulewska, K., Dominguez-Gutierrez, F. J., Kalita, D., Byggmäestar, J., Wei, G. Y., Chromiński, W., Papanikolaou, S., Alava, M. J., Kurpaska, Ł., & Jagielski, J. (2023a). Self–ion irradiation of high purity iron: Unveiling plasticity mechanisms through nanoindentation experiments and large-scale atomistic simulations. *Journal of Nuclear Materials*, *586*, 154690. https://doi.org/10.1016/j.jnucmat.2023.154690.

Mulewska, K., Rovaris, F., Dominguez-Gutierrez, F. J., Huo, W. Y., Kalita, D., Jozwik, I., Papanikolaou, S., Alava, M. J., Kurpaska, L., & Jagielski, J. (2023b). Self-ion irradiation effects on nanoindentation-induced plasticity of crystalline iron:

A joint experimental and computational study. *Nuclear Instruments and Methods in Physics Research Section B: Beam Interactions with Materials and Atoms*, *539*, 55–61. https://doi.org/10.1016/j.nimb.2023.03.004.

Muzyk, M., Nguyen-Manh, D., Kurzydłowski, K. J., Baluc, N. L., & Dudarev, S. L. (2011). Phase stability, point defects, and elastic properties of W-V and W-Ta alloys. *Physical Review B*, *84*(10), 104115. https://doi.org/10.1103/PhysRevB.84.104115.

Naghdi, A., Dominguez-Gutierrez, F. J., Huo, W. Y., Karimi, K., & Papanikolaou, S. (2022). *Dynamic nanoindentation and short-range order in equiatomic NiCoCr medium entropy alloy lead to novel density wave ordering*. arXiv. https://doi.org/10.48550/arXiv.2211.05436.

Ohser-Wiedemann, R., Martin, U., Müller, A., & Schreiber, G. (2013). Spark plasma sintering of Mo–W powders prepared by mechanical alloying. *Journal of Alloys and Compounds*, *560*, 27–32. https://doi.org/10.1016/j.jallcom.2013.01.142.

Ojha, A., Sehitoglu, H., Patriarca, L., & Maier, H. J. (2014). Twin nucleation in Fe-based bcc alloys – modeling and experiments. *Modelling and Simulation in Materials Science and Engineering*, *22*(7), 075010. https://doi.org/10.1088/0965-0393/22/7/075010.

Oliver, W. C., & Pharr, G. M. (1992). An improved technique for determining hardness and elastic modulus using load and displacement sensing indentation experiments. *Journal of Materials Research*, *7*(6), 1564–1583. https://doi.org/10.1557/JMR.1992.1564.

Papanikolaou, S., Dimiduk, D. M., Choi, W., Sethna, J. P., Uchic, M. D., Woodward, Ch. F., & Zapperi, S. (2012). Quasi-periodic events in crystal plasticity and the self-organized avalanche oscillator. *Nature*, *490*(7421), 517–521. https://doi.org/10.1038/nature11568.

Papanikolaou, S., Song, H., & Van der Giessen, E. (2017). Obstacles and sources in dislocation dynamics: Strengthening and statistics of abrupt plastic events in nanopillar compression. *Journal of the Mechanics and Physics of Solids*, *102*, 17–29. https://doi.org/10.1016/j.jmps.2017.02.004.

Pathak, S., & Kalidindi, S. R. (2015). Spherical nanoindentation stress–strain curves. *Materials Science and Engineering: R: Reports*, *91*, 1–36. https://doi.org/10.1016/j.mser.2015.02.001.

Pathak, S., Riesterer, J. L., Kalidindi, S. R., & Michler, J. (2014). Understanding pop-ins in spherical nanoindentation. *Applied Physics Letters*, *105*(16), 161913. https://doi.org/10.1063/1.4898698.

Pitts, R. A., Carpentier, S., Escourbiac, F., Hirai, T., Komarov, V., Lisgo, S., Kukushkin, A. S., Loarte, A., Merola, M., Sashala Naik, A., Mitteau, R., Sugihara, M., Bazylev, B., & Stangeby, P. C. (2013). A full tungsten divertor for ITER: Physics issues and design status. *Journal of Nuclear Materials*, *438*, S48–S56. https://doi.org/10.1016/j.jnucmat.2013.01.008.

Pöhl, F. (2019). Pop-in behavior and elastic-to-plastic transition of polycrystalline pure iron during sharp nanoindentation. *Scientific Reports*, *9*(1), 15350. https://doi.org/10.1038/s41598-019-51644-5.

Remington, T. P., Ruestes, C. J., Bringa, E. M., Remington, B. A., Lu, C. H., Kad, B., & Meyers, M. A. (2014). Plastic deformation in nanoindentation of tantalum: A new mechanism for prismatic loop formation. *Acta Materialia*, *78*, 378–393. https://doi.org/10.1016/j.actamat.2014.06.058.

Sahoo, P. K., Srivastava, S. K., Kamal, S. S. K., & Durai, L. (2015). Consolidation behavior of W–20–40 wt.% Mo nanoalloys synthesized by thermal decomposition method. *International Journal of Refractory Metals and Hard Materials*, *51*, 124–129. https://doi.org/10.1016/j.ijrmhm.2015.03.008.

Salonen, E., Järvi, T., Nordlund, K., & Keinonen, J. (2003). Effects of the surface structure and cluster bombardment on the self-sputtering of molybdenum. *Journal of Physics: Condensed Matter*, *15*(34), 5845. https://doi.org/10.1088/0953-8984/15/34/314.

Schuh, Ch. A. (2006). Nanoindentation studies of materials. *Materials Today*, *9*(5), 32–40. https://doi.org/10.1016/S1369-7021(06)71495-X.

Song, H., Dimiduk, D., & Papanikolaou, S. (2019a). Universality class of nanocrystal plasticity: Localization and self-organization in discrete dislocation dynamics. *Physical Review Letters*, *122*(17), 178001. https://doi.org/10.1103/PhysRevLett.122.178001.

Song, H., Yavas, H., Van der Giessen, E., & Papanikolaou, S. (2019b). Discrete dislocation dynamics simulations of nanoindentation with pre-stress: Hardness and statistics of abrupt plastic events. *Journal of the Mechanics and Physics of Solids*, *123*, 332–347. https://doi.org/10.1016/j.jmps.2018.09.005.

Stukowski, A. (2010). Visualization and analysis of atomistic simulation data with OVITO-the Open Visualization Tool. *Modelling and Simulation in Materials Science and Engineering*, *18*(1). https://doi.org/10.1088/0965-0393/18/1/015012.

Stukowski, A., Bulatov, V. V., & Arsenlis, A. (2012). Automated identification and indexing of dislocations in crystal interfaces. *Modelling and Simulation in Materials Science and Engineering*, *20*(8), 085007. https://doi.org/10.1088/0965-0393/20/8/085007.

Tao, H., Li, J., Li, J., Hou, Z., Yang, X., & Fan, L.-Z. (2022). Metallic phase $W_{0.9}Mo_{0.1}S_2$ for high-performance anode of sodium ion batteries through suppressing the dissolution of polysulfides. *Journal of Energy Chemistry*, *66*, 356–365. https://doi.org/10.1016/j.jechem.2021.08.026.

Thompson, A. P., Aktulga, H. M., Berger, R., Bolintineanu, D. S., Brown, W. M., Crozier, P. S., Veld, P. J., in 't, Kohlmeyer, A., Moore, S. G., Nguyen, T. D., Shan, R., Stevens, M. J., Tranchida, J., Trott, Ch., & Plimpton, S. J. (2022). LAMMPS – a flexible simulation tool for particle-based materials modeling at the atomic, meso, and continuum scales. *Computer Physics Communications*, *271*, 108171. https://doi.org/https://doi.org/10.1016/j.cpc.2021.108171.

Turchi, P., Drchal, V., Kudrnovský, J., Colinet, C., Kaufman, L., & Liu, Z.-K. (2005). Application of *ab initio* and CALPHAD thermodynamics to Mo-Ta-W alloys. *Physical Review B*, *71*(9), 094206. https://doi.org/10.1103/PhysRevB.71.094206.

Varillas, J. (2019). *A Molecular Dynamics Study of Nanocontact Plasticity and Dislocation Avalanches in FCC and BCC Crystals* [Ph.D. thesis]. University of West Bohemia. https://doi.org/10.13140/RG.2.2.13904.87040.

Varillas, J., Očenášek, J., Torner, J., & Alcalá, J. (2017). Unraveling deformation mechanisms around FCC and BCC nano-contacts through slip trace and pileup topography analyses. *Acta Materialia*, *125*, 431–441. https://doi.org/10.1016/j.actamat.2016.11.067.

Wang, X., Xu, S., Jian, W.-R., Li, X.-G., Su, Y., & Beyerlein, I. J. (2021). Generalized stacking fault energies and peierls stresses in refractory body-centered cubic metals from machine learning-based interatomic potentials. *Computational Materials Science*, *192*, 110364. https://doi.org/10.1016/j.commatsci.2021.110364.

Wei, G., Byggmästar, J., Cui, J., Nordlund, K., Ren, J., & Djurabekova, F. (2023). Effects of lattice and mass mismatch on primary radiation damage in W–Ta and W–Mo binary alloys. *Journal of Nuclear Materials*, *583*, 154534. https://doi.org/10.1016/j.jnucmat.2023.154534.

Wurster, S., Gludovatz, B., Hoffmann, A., & Pippan, R. (2011). Fracture behaviour of tungsten–vanadium and tungsten–tantalum alloys and composites. *Journal of Nuclear Materials*, *413*(3), 166–176. https://doi.org/10.1016/j.jnucmat.2011.04.025.

Wyszkowska, E., Mieszczynski, C., Kurpaska, Ł., Azarov, A., Jóźwik, I., Kosińska, A., Chromiński, W., Diduszko, R., Huo, W. Y., Cieślik, I., & Jagielski, J. (2023). Tuning heterogeneous ion-radiation damage by composition in NiFe binary single crystals. *Nanoscale*, *15*, 4870–4881. https://doi.org/10.1039/D2NR06178C.

Xiong, K., Liu, X., & Gu, J. (2014). Orientation-dependent crystal instability of gamma-TiAl in nanoindentation investigated by a multiscale interatomic potential finite-element model. *Modelling and Simulation in Materials Science and Engineering*, *22*(8), 085013. https://doi.org/10.1088/0965-0393/22/8/085013.

Xiong, K., Lu, H., & Gu, J. (2016). Atomistic simulations of the nanoindentation-induced incipient plasticity in Ni$_3$Al crystal. *Computational Materials Science*, *115*, 214–226. https://doi.org/10.1016/j.commatsci.2015.12.045.

Xu, Q., Zaborowska, A., Mulewska, K., Huo, W., Karimi, K., Domínguez-Gutiérrez, F. J., Kurpaska, Ł., Alava, M. J., & Papanikolaou, S. (2023). Atomistic insights into nanoindentation-induced deformation of α-Al$_2$O$_3$ single crystals. *Vacuum*, *219*(A), 112733. https://doi.org/10.1016/j.vacuum.2023.112733.

Xu, R.-G., Song, H., Leng, Y., & Papanikolaou, S. (2021). A molecular dynamics simulations study of the influence of prestrain on the pop-in behavior and indentation size effect in cu single crystals. *Materials*, *14*(18), 5220. https://doi.org/10.3390/ma14185220.

Xu, S., Hwang, E., Jian, W.-R., Su, Y., & Beyerlein, I. J. (2020). Atomistic calculations of the generalized stacking fault energies in two refractory multi-principal element alloys. *Intermetallics*, *124*, 106844. https://doi.org/10.1016/j.intermet.2020.106844.

Yin, B., Maresca, F., & Curtin, W. A. (2020). Vanadium is an optimal element for strengthening in both fcc and bcc high-entropy alloys. *Acta Materialia*, *188*, 486–491. https://doi.org/10.1016/j.actamat.2020.01.062.

Yu, H., Das, S., Yu, H., Karamched, P., Tarleton, E., & Hofmann, F. (2020). Orientation dependence of the nano-indentation behaviour of pure tungsten. *Scripta Materialia*, *189*, 135–139. https://doi.org/10.1016/j.scriptamat.2020.08.014.

Zhang, X., Tang, J., Deng, L., Zhong, G., Liu, X., Li, Y., Deng, H., & Hu, W. (2017). The effects of interstitial impurities on the mechanical properties of vanadium alloys: A first-principles study. *Journal of Alloys and Compounds*, *701*, 975–980. https://doi.org/10.1016/j.jallcom.2017.01.135.